Commun. Comput. Phys.
doi: 10.4208/cicp.160114.120914a

Vol. **17**, No. 2, pp. 401-423
February 2015

Computationally Efficient Fluid-Particle Dynamics Simulations of Arterial Systems

Tejas S. Umbarkar[1] and Clement Kleinstreuer[1,2,*]

[1] *Mechanical & Aerospace Engineering Department, North Carolina State University, Raleigh, NC 27695, USA.*
[2] *Joint Department of Biomedical Engineering, North Carolina State University and University of North Carolina at Chapel Hill, Raleigh, NC 27695, USA.*

Received 16 January 2014; Accepted (in revised version) 12 September 2014

Communicated by Peter Jimack

Abstract. Realistic and accurate computer simulations of the particle-hemodynamics in arterial systems can be a valuable tool for numerous biomedical applications. Examples include optimal by-pass grafting and optimal drug-delivery, as well as best medical management concerning the cardio-vascular system. However, such numerical analyses require large computer resources which may become prohibitive for extended sets of arterial bifurcations. A remedy is to develop a hybrid model where the first few generations of the bifurcating arteries of interest are simulated in full 3-D, while a 1-D model is then coupled for subsequent bifurcations. Alternatively, a 1-D computer model can be directly employed to simulate fluid-particle transport in complex bifurcating networks.

Relying on a representative axial velocity profile, a physiological 1-D model has been developed and validated, which is capable of predicting with reasonable accuracy arterial flow, pressure field and elastic wall interaction as well as particle transport. The usefulness of the novel 1-D simulation approach is demonstrated via a comparison to 3-D blood flow and microsphere transport in a hepatic artery system, featuring as outlets one major branch and four small daughter vessels. Compared to the 3-D simulation, the 1-D analysis requires only about 1% of computational time. The hybrid modeling approach would be also applicable to the human respiratory tract to evaluate the fate of inhaled aerosols.

A simple and cost-effective way to simulate particle-hemodynamics is using a 1-D model for simulating arterial pressures and flow rates as well as microsphere transport, based on assumptions involving the use of a simple algebraic pressure-area relation, an exponential elasticity model for the vessels, and considering only unidirectional flow with a representative skewed velocity profile. In summary, the novel contributions are:

*Corresponding author. *Email addresses:* tumbark@ncsu.edu (T. S. Umbarkar), ck@ncsu.edu (C. Kleinstreuer)

 ©2015 Global-Science Press

https://doi.org/10.4208/cicp.160114.120914a Published online by Cambridge University Press

- Particle tracking in arteries via 1-D fluid modeling and selection of an averaged, skewed velocity profile based on 3-D simulation results to provide more realistic friction and inertia term values for modeling a flow system with bifurcations.
- The 1-D model can be coupled to a 3-D model so that simulations can be run for larger regions of vascular or lung-airway systems.

AMS subject classifications: 70-08

Key words: 1-D modeling, skewed representative velocity profile, fluid-structure interaction, particle tracking.

1 Background and information

A novel technique for optimal targeting of drugs onto solid tumors has been proposed by Kleinstreuer et al. [1] and further numerically analyzed for liver tumors [2]. For realistic and accurate computer simulations it has to be assumed that the geometry of the vasculature is 3-D and blood flow is non-Newtonian, transient, laminar and incompressible. Also, the drug-particles in dilute suspensions are spherical and non-interacting; but, the walls of the arteries are flexible, giving rise to the need of proper fluid-structure interaction. These fluid-particle dynamics simulations require high computational time and cost, even for only a few generations. Thus, simulating arterial flow and pressure fields in any extended set of arterial bifurcations could be computationally prohibitive. A remedy is the development of a 3-D/1-D coupled model. In this, the first few generations of the arterial system would be simulated in full 3-D, while a 1-D model would be used for subsequent bifurcations (see Fig. 1). Alternatively, a 1-D computer model can be employed to simulate fluid-particle transport in complex bifurcating networks *directly*.

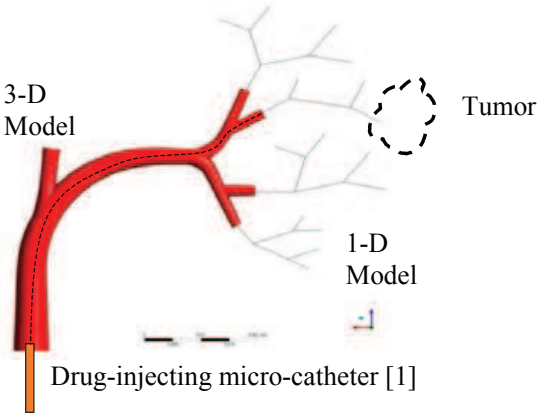


Figure 1: Sample application of a coupled 3-D/1-D model for direct tumor-targeting.

https://doi.org/10.4208/cicp.160114.120914a Published online by Cambridge University Press

In summary, in this study a physiological 1-D model is developed and validated, which is capable of predicting arterial flow, pressure field and particle transport with reasonable accuracy. The hybrid modeling approach would be also applicable to the human respiratory tract to analyze the fate of inhaled toxic or therapeutic aerosols. The model is first derived from basic equations and particle tracking is augmented. In the later sections, we validate this model against published data and then test its application against a 3-D fluid-particle simulation of the hepatic artery system.

Computational analyses of human circulatory and pulmonary systems have been previously established to gain further physical insight and for their applications concerning different therapies. For example, Lin et al. [3] presented a 3-D/1-D coupled model for predicting pulmonary air flow, while Formaggia et al. [4] analyzed a 3-D/1-D coupled model for fluid flow in a compliant vessel. Several1-D models have been proposed in [5–8]. These contributions differ in terms of the variables used in the basic equations, elasticity values selected for the vessel walls, implementation of the fluid-structure interactions, and the way boundary conditions were applied.

Experimental models of arterial systems have also been employed to obtain pressure and flow waveforms, which are useful for physical insight and the validation of computer models [9–11].

A 1-D model of the arterial system requires the reduction of the Navier-Stokes equations. In addition, one has to account for the compliance of the vessels and the impact of elastic (or viscoelastic) vessel walls. The main differences between the published modeling approaches are the way in which the boundary conditions are implemented, the relation between pressure and area, as well as the discretization scheme. For example, Sherwin et al. in [12] derived the 1-D flow equations for several different combinations of variables (i.e., area-flow, area-velocity, pressure-velocity and pressure-flow). However, there are assumptions involved in deriving these types of equations; for example, the area-velocity and pressure-velocity forms assume inviscid flow while the pressure-flow form assumes constant material properties. Thus, the area-flow form is the most general form and was selected for this study as well.

Along with the governing equations, an important component is the fluid-structure interaction (FSI) model, as the arteries are flexible and their cross-sectional areas vary with the local pressure. Formaggia et al. [6] provided a comprehensive relation between the pressure and the area of the vessel in terms of a partial differential equation representing the mechanical model for wall displacement:

$$\rho_w h_0 \frac{\partial^2 \eta}{\partial t^2} - \gamma \frac{\partial \eta}{\partial t} - \alpha \frac{\partial^3 \eta}{\partial t \partial z^2} + b\eta = p - p_{ext}. \tag{1.1}$$

Here, the first term represents the inertia term, the second term is a Voigt-type viscoelasticity, the third term is related to the longitudinal pre-stress, the fourth one is another viscoelastic term, and the last one is the elastic response function. They later conclude that a simple algebraic p-A relation derived from the above expression is also able to capture the physiological wall distensibility within the limits of physiological values of pres-

https://doi.org/10.4208/cicp.160114.120914a Published online by Cambridge University Press

sure, wall displacement, and velocities. A similar algebraic relation was also employed in [5, 12, 13]. For accounting the change in elasticity with radius, Olufsen et al. [14] used an exponential relation between elasticity and radius.

Different numerical schemes like discontinuous Galerkin scheme, second-order Taylor-Galerkin scheme [6], two-step Lax-Wendroff scheme [5, 15] and finite difference McCormack scheme [16] have been employed for solving the system of equations.

Boundary conditions (BCs) are necessary to gain closure. The bifurcation conditions decide the pressure and flow distribution across a bifurcation. Generally, Bernoulli's law and mass conservation, or pressure continuity and mass conservation, are used as the bifurcation boundary conditions (see [12, 14]). Formaggia et al. [6] also provided a method to account for the angles of bifurcating vessels. Reflection coefficients have been used in [17, 18].

Even a 1-D model has to be terminated at a certain point downstream and appropriate outflow BCs should be used in order to capture the influence of the remaining vasculature. Thus, appropriate BCs should account for wave propagation and reflection phenomena. A general approach is to represent the downstream vasculature by a Windkessel model.

2 Model description

The process of building the 1-D model consists of several implementation steps, including the system of transport equations for fluid-particle flow and FSI, the boundary conditions, and the numerical scheme.

2.1 System of flow equations

The full Navier-Stokes equations are simplified to 1-D based on necessary assumptions and averaged quantities. The artery is assumed to be a flexible tube with circular cross-section at all times. The vessel wall is longitudinally tethered and hence the length L of the vessel is fixed. The cylindrical co-ordinate system is used where $R(x,t)$ is the radius of the vessel, $A(x,t)$ is the area, and $p(x,t)$ is the pressure at axial position x within the vessel. The density, ρ, and the viscosity, μ, are constant. Starting out with the velocity vector in the tube as $\vec{u}[u_r(r,x,t),u_x(r,x,t)]$, where u_r is the radial component and u_x is the axial component, the continuity equation reduces to:

$$\frac{\partial u_x}{\partial x}+\frac{1}{r}\frac{\partial}{\partial r}(ru_r)=0. \tag{2.1}$$

To obtain the 1-D form, Eq. (2.1) is integrated over the vessel cross-section:

$$2\pi\int_0^R\Big(\frac{\partial u_x}{\partial x}+\frac{1}{r}\frac{\partial}{\partial r}(ru_r)\Big)rdr=0.$$

https://doi.org/10.4208/cicp.160114.120914a Published online by Cambridge University Press

Integrating by parts and simplification yields [19]:

$$\frac{\partial Q}{\partial x}+\frac{\partial A}{\partial t}=0. \tag{2.2}$$

The momentum equation for transient axisymmetric flow reads:

$$\frac{\partial u_x}{\partial t}+u_x\frac{\partial u_x}{\partial x}+u_r\frac{\partial u_x}{\partial r}+\frac{1}{\rho}\frac{\partial p}{\partial x}=\frac{\nu}{r}\frac{\partial}{\partial r}\left(\frac{r\partial u_x}{\partial r}\right). \tag{2.3}$$

Here, the axial viscosity term has been neglected as it is very small compared to the right hand side. Integrating over the cross-section results in:

$$2\pi\int_0^R\frac{\partial u_x}{\partial t}rdr+2\pi\int_0^R\left(u_x\frac{\partial u_x}{\partial x}+u_r\frac{\partial u_x}{\partial r}\right)rdr+\frac{A}{\rho}\frac{\partial p}{\partial x}=2\pi\nu\left[\frac{r\partial u_x}{\partial r}\right]_R. \tag{2.4}$$

Again, integrating by parts and simplifying using the continuity equation yields:

$$\frac{\partial Q}{\partial t}+\frac{1}{Au^2}\iint_A u_x^2dA*Au^2+\frac{A}{\rho}\frac{\partial p}{\partial x}=2\pi\nu\left[\frac{r\partial u_x}{\partial r}\right]_R. \tag{2.5}$$

The term $\frac{1}{Au^2}\iint_A u_x^2dA$ is the momentum correction factor and $2\pi\nu\left[\frac{r\partial u_x}{\partial r}\right]_R$ represents axial friction. Being faced with more unknowns than equations, an appropriate cross-sectional velocity profile is needed. Earlier works (e.g., [5, 12, 13]) employed a uniform velocity profile, which is unrealistic especially for flow in bifurcating vessels. As the momentum correction factor and the friction term depend on the velocity profile (see Eq. (2.5)), using a skewed velocity profile will generate more realistic modeling results. As most of the bifurcations encountered in our 3-D system would be asymmetric, a representative fluid-flow distribution was selected based on the velocity profile from a 3-D simulation of an asymmetric bifurcation, as shown in Fig. 2 (see [20]).

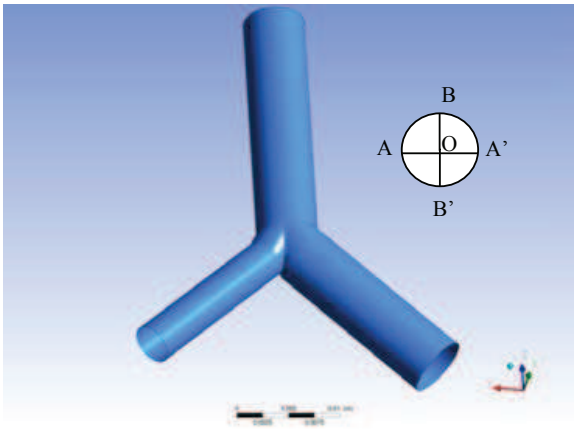


Figure 2: Geometry used for extracting a realistic axial velocity profile.

https://doi.org/10.4208/cicp.160114.120914a Published online by Cambridge University Press

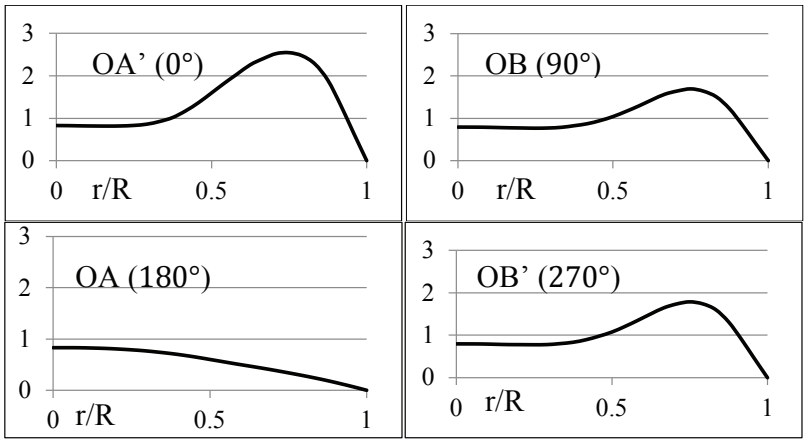


Figure 3: Average normalized velocity profiles at different angular positions.

First, the velocity profiles were recorded at the mid-plane of the smaller vessel along the four lines OA, OA', OB and OB'. The velocity profiles were normalized by the average velocity of all the four angular positions, while the radius was normalized with the pipe radius. A similar procedure was followed for the larger vessel. A representative velocity profile was then calculated by taking the average of the corresponding velocity profiles in the large and small (daughter) vessels. Fig. 3 shows these average normalized velocity profiles in terms of u/u_{avg} vs. r/R, where R is the pipe radius.

All these profiles were then fitted with a ninth degree polynomial (this gave an accurate fit and being a polynomial, is easy to manipulate in later stages of calculations) with the help of MAPLE 13. In order to obtain the complete velocity profile in terms of the normalized radius and the angular variable theta (θ), interpolation was used [21]. Knowing the velocity profiles at the four locations, a smooth function $u/u_{avg}(r/R,\theta)$ can be determined in the cylindrical co-ordinate system follows:

$$\bar{u}(\bar{r},\theta)=g_1(\bar{r})+g_2(\bar{r})\cos(2\theta)+g_3(\bar{r})\sin(\theta)+g_4(\bar{r})\cos(\theta), \tag{2.6}$$

with

$$g_1(\bar{r})=\frac{1}{4}\left[\bar{u}(\bar{r},0)+\bar{u}\left(\bar{r},\frac{\pi}{2}\right)+\bar{u}(\bar{r},\pi)+\bar{u}\left(\bar{r},\frac{3\pi}{2}\right)\right], \tag{2.7}$$

$$g_2(\bar{r})=\frac{1}{4}\left[\bar{u}(\bar{r},0)-\bar{u}\left(\bar{r},\frac{\pi}{2}\right)+\bar{u}(\bar{r},\pi)-\bar{u}\left(\bar{r},\frac{3\pi}{2}\right)\right], \tag{2.8}$$

$$g_3(\bar{r})=\frac{1}{4}\left[\bar{u}\left(\bar{r},\frac{\pi}{2}\right)-\bar{u}\left(\bar{r},\frac{3\pi}{2}\right)\right], \tag{2.9}$$

$$g_4(\bar{r})=\frac{1}{4}[\bar{u}(\bar{r},0)-\bar{u}(\bar{r},\pi)], \tag{2.10}$$

and

$$\bar{u}=\frac{u}{u_{avg}},\quad \bar{r}=\frac{r}{R}.$$

https://doi.org/10.4208/cicp.160114.120914a Published online by Cambridge University Press

Once the velocity profile is known, one can proceed to calculate the friction term and the momentum correction factor. As a result, the modified momentum equation now reads:

$$\frac{\partial Q}{\partial t}+1.63789\frac{\partial}{\partial x}\left(\frac{Q^2}{A}\right)+\frac{A}{\rho}\frac{\partial p}{\partial x}=-14.99647\pi\nu\frac{Q}{A}. \tag{2.11}$$

Eqs. (2.2) and (2.11) are the continuity and momentum equation in 1-D, respectively. We observe that in the above system, there are two equations but three variables (A,Q,p). The third equation is a state equation which provides the relation between the area and pressure in the vessel (FSI). The algebraic relation used in [5] is:

$$p(x,t)-p_0=\frac{4}{3}\frac{Eh}{r_0}\left(1-\frac{\sqrt{A_0}}{\sqrt{A}}\right), \tag{2.12}$$

where p_0, r_0 and A_0 are the pressure, radius and area at zero transmural pressure, (i.e. at diastole) respectively. Olufsen in [5] assumed the arteries to be tapering thin-walled vessels and then the internal and external forces are balanced in the radial direction to obtain the above relation between the pressure and the cross-sectional area. The same relation has been employed in the present model.

Stergiopulos et al. [22] have published data for the volume compliance of various human arteries. From this data Olufsen derived an expression for the combined parameter Eh/r_0 as [5]:

$$\frac{Eh}{r_0}=2*10^6\exp(-2253*r_0)+8.65*10^4 Pa. \tag{2.13}$$

Knowing the p-A relationship, Eqs. (2.2) and (2.11) can be solved, considering that human arteries taper along their length. To account for this fact, radial vessel variations are assumed to follow Eq. (2.14):

$$r(x)=r_{in}\left(\frac{r_{out}}{r_{in}}\right)^{\frac{x}{L}}, \tag{2.14}$$

where $r(x)$ is the (base) radius at any point along the length x of the vessel, r_{in} is the inlet radius, r_{out} is the outlet radius, and L is the length of the vessel. Eqs. (2.13) and (2.14) are used as additional physiological models.

An approach is given by Martin et al. [33], where the authors use optimization to fit a 1-D model to 3-D results and obtain certain parameters in the 1-D model. This approach is a possible way of proceeding; however, the parameters thus obtained would be more specific to the 3-D results and the 1-D model would have a lesser physiological relevance.

2.2 Boundary conditions

Boundary conditions are required for the inlet and outlets, while the bifurcations require matching conditions. We must first find the values of the variables at all the boundaries to be able to calculate the flow field in the interior. The inlet boundary condition is fairly

https://doi.org/10.4208/cicp.160114.120914a Published online by Cambridge University Press

straightforward as the inlet values for either mean velocity or flow rate should be known from either patient specific or population averaged data.

The basic concept for the bifurcation conditions is the conservation of mass flow. For incompressible fluids, the flow rate at the end of a parent vessel is equal to the sum of the flow rates at the inlet of the daughters, at any point of time. At the same time, pressure has to be the same at the outlet of the parent vessel and the inlet of the daughter vessels.

In [14], the authors employed the structured tree outlet BC. They claimed that this BC is a physiologically correct BC and is better than the generally used Windkessel BC as it is able to capture the reflected waves effectively and hence can maintain a 'phase lag' between the pressure and flow. The structured tree may also capture high frequency oscillations [23]. However, the Windkessel model is much easier to use and gives physiological results very similar to those obtained with the structured tree BC [19]. This work employs the three element Windkessel model (WK3) for which the pressure and flow are related as [19]:

$$R_u\frac{dQ}{dt}=\frac{dp}{dt}+\frac{p}{CR_d}-\frac{1}{C}\left(1+\frac{R_u}{R_d}\right)Q, \tag{2.15}$$

where Q is the flow rate through the system, being replaced by the WK3, and p is the pressure.

2.3 Numerical scheme

The two step Lax-Wendroff scheme was selected for its simplicity [14]. It is a second-order method in both space and time. For a system in the form:

$$\frac{\partial}{\partial t}U+\frac{\partial}{\partial x}R=S. \tag{2.16}$$

The system of equations obtained by substituting Eq. (2.12) in Eq. (2.11), along with Eq. (2.2) is in the above form, where U is the vector of unknowns (Q and A) while R and S can be obtained by writing the system in form of Eq. (2.16).

The two step Lax-Wendroff scheme, as applied to our system, is:

$$U_i^{n+1}=U_i^{n+1}-\frac{\Delta t}{\Delta x}\left(R_{i+\frac{1}{2}}^{n+\frac{1}{2}}-R_{i-\frac{1}{2}}^{n+\frac{1}{2}}\right)+\frac{\Delta t}{2}\left(S_{i+\frac{1}{2}}^{n+\frac{1}{2}}+S_{i-\frac{1}{2}}^{n+\frac{1}{2}}\right) \qquad \text{(Step 1)}, \tag{2.17}$$

$$U_j^{n+\frac{1}{2}}=\frac{U_{j+\frac{1}{2}}^{n+\frac{1}{2}}+U_{j-\frac{1}{2}}^{n+\frac{1}{2}}}{2}+\frac{\Delta t}{2}\left(\frac{R_{j+\frac{1}{2}}^{n}-R_{j+\frac{1}{2}}^{n}}{\Delta x}+\frac{S_{j+\frac{1}{2}}^{n}+S_{j+\frac{1}{2}}^{n}}{2}\right) \qquad \text{(Step 2)}, \tag{2.18}$$

for $j=i+1/2$ and $j=i-1/2$.

The code has been written in FORTRAN 95 (Microsoft Visual Studio 2005). The choice of the coding language was made based on the ease of incorporation into commercial CFD-packages like ANSYS CFX or Fluent for further processing. All the vessels are divided into an equal number of parts, and flow and pressure are calculated for each of these parts.

https://doi.org/10.4208/cicp.160114.120914a Published online by Cambridge University Press

2.4 Particle dynamics equations

Broadly, there are two ways to model particle transport, i.e., the Eulerian-Eulerian model for nano-spheres, or the Euler-Lagrange approach for micron particles. The Eulerian approach is discussed by Quarteroni et al. [34]. They integrate the advection-diffusion equation over the flow cross-section. However, this approach is unable to provide temporal information, i.e., the distance travelled after certain time or the velocity of particles, as it deals only with particle concentrations. In regard to microspheres, which are used in the present simulations, a Euler-Lagrange model is more appropriate. This approach enables us to track the individual particles (i.e., their velocities and locations) in time.

One-way coupling is assumed because the particle concentration is low, i.e., a dilute suspension is assumed. This model considers the point forces acting on each particle to determine its position and velocity. In general, these forces include surface forces like drag, pressure, Basset, lift and interaction forces as well as volume forces such as gravity and virtual mass [35].

The Basset history force is negligible when the particle relaxation time is less than the transient system's period. In our case, the maximum possible particle relaxation time is about 10^{-4} seconds [24,29] while the transient system's period, i.e. the time period of the pulse is about 1 second. Thus the Basset history force can be neglected. Simulations on a representative geometry conducted with and without the virtual mass force show that this force can be neglected [24, 29]. Regions of high shear like flow-separation regions are the regions where the lift force is significant. It is also important when the relative velocity between the particles and fluid is higher. Since the high shear regions are a small part of our domain and we expect the relative velocity of the particles to be very small, the lift force is also neglected. Finally, because we are assuming a dilute suspension, the interaction forces between the particles are neglected as well.

In modeling the motion of particles for horizontal flow, gravity need not be considered, and hence only the drag and pressure forces are applicable. Thus, Newton's Second Law for each particle reads:

$$m_p \frac{dv_p}{dt} = F_{drag} + F_{pressure}. \tag{2.19}$$

Here m_p is the particle mass, v_p is the particle velocity, F_{drag} is the drag force, and $F_{pressure}$ is the pressure force. The drag force is exerted on the particle surface because of fluid-particle velocity differences, while the pressure force arises due to the pressure gradient across the particle surface. Specifically,

$$F_{drag} = \frac{1}{8}\pi\rho_p d_p^2 C_d (v_f - v_p)|v_f - v_p|, \tag{2.20}$$

where [25]

$$C_d = \frac{24}{Re_p}(1 + 0.15 Re_p^{0.687}) \tag{2.21}$$

https://doi.org/10.4208/cicp.160114.120914a Published online by Cambridge University Press

and

$$Re_p = \frac{\rho_f |v_f - v_p| d_p}{\mu}. \tag{2.22}$$

The pressure force is:

$$F_{pressure} = -d_p^3 \frac{\pi}{6} \nabla p. \tag{2.23}$$

Here, d_p is the particle diameter, v_f is the fluid velocity, v_p is the particle velocity, ρ_f is the fluid density, C_d is the drag coefficient, Re_p is the particle Reynolds number, and p is the fluid pressure. We observe that the pressure force acts in a direction opposite to that of the pressure gradient. Thus, the final equation in 1-D reads:

$$m_p \frac{dv_p}{dt} = \frac{1}{8} \pi \rho_p d_p^2 C_d (v_f - v_p) |v_f - v_p| - d_p^3 \frac{\pi}{6} \frac{\partial p}{\partial x}. \tag{2.24}$$

Use of the Lagrangian model in 1-D is quite different. As we have only one velocity which is the average cross-sectional velocity, this is the only velocity driving the particles. Also, from the above equation we see that if the mass and diameter of two particles are the same, they will have the same velocity. This implies that if we have a system consisting of particles of the same density and having equal diameters, all of the particles will have the same velocity (in 1-D) as long as they are released with same initial velocity. It would be as if they are moving together as a cluster.

As a simple first approach, a forward difference scheme is used for the particle velocity derivative. The pressure gradient across the particle surface is governed by the previous position of the particle. The pressure gradient is calculated from the difference in the pressure at the previous point and the point next to it, i.e. forward difference in space.

As is seen from Eq. (2.24), the only unknowns in finding the particle velocity are the fluid velocity and pressure. These are obtained from the solution of the continuity and momentum equation. In a way, particle tracking can be considered as a part of post-processing for a particular time step. First the fluid dynamic calculations are done and the fluid velocities and pressures are determined at all the grid points. Next, from these values, using the discretized form of Eq. (2.24), particle velocities are computed. These particle velocities are instantaneous velocities. The distance traveled by the particle during that time step can be found out by multiplying the particle velocity by the time step (Δt) in which the velocity was obtained. The axial position of the particle in the vessel at a particular time is calculated by adding up all such distances traveled by the particle until that time.

2.5 Particle distribution across bifurcations

In 3D simulations, the motion of the particles along the co-ordinate axes is governed by the corresponding fluid velocities. This results in a 3D particle motion which leads to the particle entering a particular vessel at a bifurcation. Thus, which daughter vessel the

https://doi.org/10.4208/cicp.160114.120914a Published online by Cambridge University Press

particle would enter depends on the forces acting on the particle. However, in 1-D, there is only one velocity which is along the axis of the vessel. The particle experiences forces only in the axial direction. This raises a question about the criteria based on which the particle would enter a particular daughter vessel at the bifurcation. In [20] the authors conducted bench-top experiments regarding this. They release particles of diameters 0.6 mm, 1.6 mm and 3.2 mm in a rigid vessel (6 mm diameter) and studied their distribution across a bifurcation. The two branching conduits have unequal radii and the flow rate in each is prescribed in terms of a fraction of the parent vessel flow rate. After observing the particle distribution in the two daughter vessels for multiple ratios of flow rates in them, they conclude that smaller particles (with diameters 0.6 mm and 1.6 mm) are distributed in the ratio of the flow rates in the daughter vessels.

The particles which we would be dealing with in our 1-D model would be around 32 microns and the typical diameter of the vessels would be 1 mm. Comparing this size to that used in [20], we can say that we have the case of 'smaller' particles and that we can use the particle bifurcation condition that they are distributed in the ratio of the flow rates. Clearly, we would know the total number of particles entering the system at the beginning. The velocity and acceleration of the particles would be governed by the two forces. When they encounter a bifurcation, they would be divided between the branches with the ratio of the flow rates in the respective daughters, and hence we would know the number of particles entering each daughter vessel.

Once we have the particle velocity, we can easily find out its axial position in the vessel knowing the time and can predict the approximate time taken by the particles to reach a possible end point or embolization spot.

3 Model validations

3.1 Validation with experimental/computational observations by Kung et al. (2011) [9]

In this experimental paper, the authors have compared the simulated results from a 3-D model of a single compliant vessel with experimental data obtained for the same vessel.

3.1.1 The experiment

For the experiment, a silicone compliant vessel of unpressurized radius of 2 cm, length 25 cm and wall thickness 0.08 cm was used. These parameters were chosen so as to mimic the physiological geometry of the human descending thoracic aorta. A computer controlled pump was used to give a physiological flow input to the vessel. As for the outlet, a resistance module was constructed which was then connected to the outlet of the vessel. This model was based on the four element Windkessel model (WK4) consisting of a proximal resistance (R_P), a distal resistance (R_D), a capacitance (C) and an inductance (L). The density and viscosity of the working fluid were 1050 Kg/m3 and 0.00461 Pa.s respectively. The authors used a dynamic modulus of 1 MPa for the elastic vessel.

https://doi.org/10.4208/cicp.160114.120914a Published online by Cambridge University Press

3.1.2 Present model parameters

In order to simulate the physiological input, a Fourier series with eight terms was used to approximate the flow pattern. For the outlet BC, a WK3 model was employed. The parameters used for this WK3 were based on those of WK4 and the outlet flow and pressures as given in [9]. The parameter values are from [26] for the same validation: $R_u = 28.4268 \times 10^6$ Pa.s/m^3, $R_d = 384.3939$ Pa.s/m^3 and $C = 1.384 \times 10^{-9}$ m^3/Pa.

The 1-D code was run for the above parameters and the results were compared with those obtained experimentally in [5]. Figs. 4 and 5 show the comparison between results obtained from our 1-D model and those documented in [5] from the bench-top experiment.

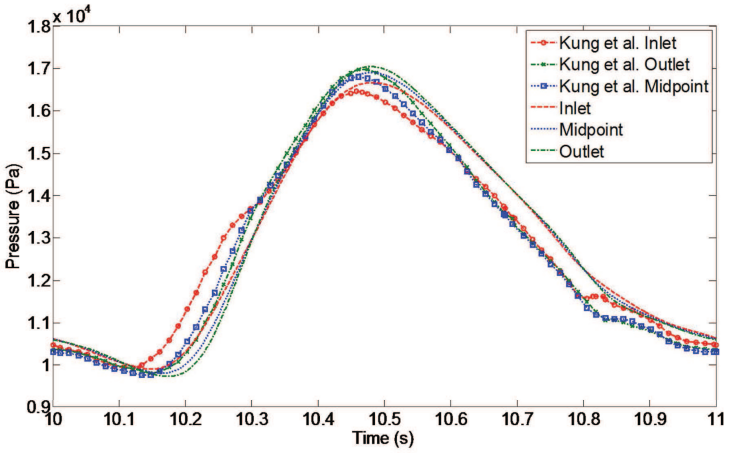


Figure 4: Pressure plot for $E = 1.2$ MPa, $r_0 = 1$ cm.

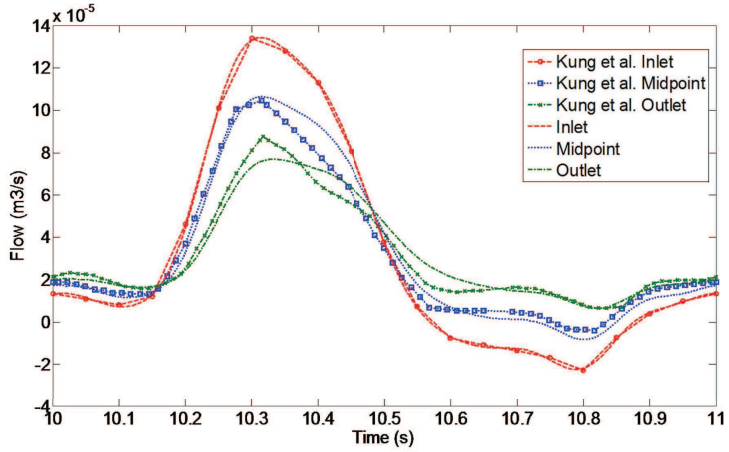


Figure 5: Flow plot for $E = 1.2$ MPa, $r_0 = 1$ cm.

https://doi.org/10.4208/cicp.160114.120914a Published online by Cambridge University Press

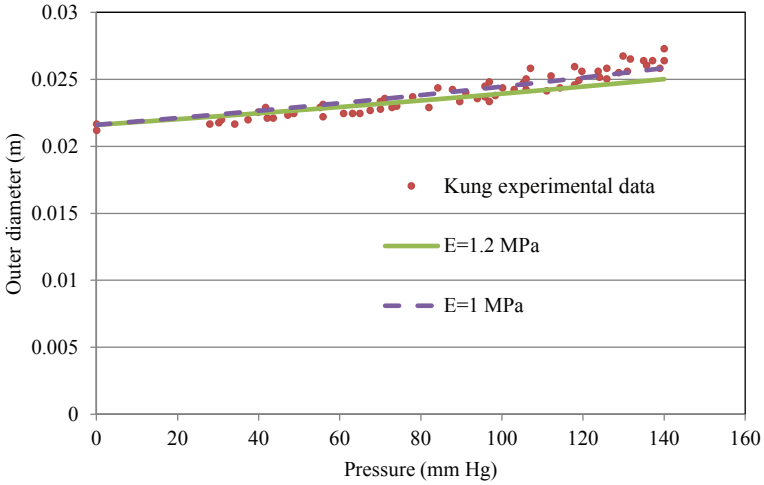


Figure 6: Comparison of pressure-diameter response with Kung et al. (2011).

The waveform converged after 7 to 8 pulses. Results shown are for the converged waveform. The time required with 50 grid points was about 25 seconds. One can see that the pressure distributions and the flow rate match rather well for an elasticity module of 1.2 MPa. A noticeable lag is seen between the maximum flow rate occurrence and maximum pressure occurrence which is physiologically correct.

When lowering the E-value to 1 MPa, it is evident from Fig. 6 that for the given physiological pressure range the trend corresponding to 1.2 MPa elasticity provides a slightly closer distensibility match than for 1 MPa elasticity.

3.2 Validation with the model by Marchandise et al. (2009) [27]

This validation focused primarily on the bifurcation boundary conditions. Their hyperbolic system of equations was in the A-u form, assuming a flat velocity profile

$$\frac{\partial A}{\partial t}+\frac{\partial (Au)}{\partial x}=0 \tag{3.1}$$

and

$$\frac{\partial u}{\partial t}+u\frac{\partial u}{\partial x}+\frac{1}{\rho}\frac{\partial p}{\partial x}+K\frac{u}{A}=0, \tag{3.2}$$

where $K=22\pi\mu$. This system is then discretized using a Discontinuous Galerkin method and a four- stage explicit Runge-Kutta scheme. They used their model to predict the flows and pressures in a single bifurcation and validated it against the calculations done in [12].

Specifically, the parent vessel had a length of 20 cm and a radius of 0.5 cm while the daughters had lengths of 20 cm and radius of 0.2041 cm each. The radii of the daughters

https://doi.org/10.4208/cicp.160114.120914a Published online by Cambridge University Press

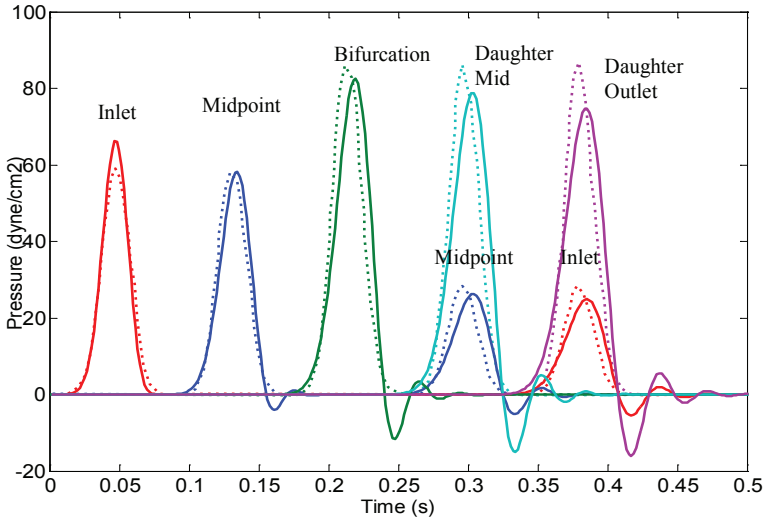


Figure 7: Pressure plots from 1-D and those of Marchandise et al. (2009). Solid-simulation, dotted- Marchandise et al. (2009).

were selected so as to get a reflection coefficient of 0.5 for the bifurcation [12]. This would mean that at the bifurcation, the magnitude of the reflected wave would be half of that of the incident wave. Also, for this case the viscosity was set to zero to simplify the analysis. At the inlet, the inflow velocity was specified. The transient inflow velocity was in the form of a Gaussian bell curve:

$$u(0,t)=0.5\exp\left(-5000(t-0.05)^2\right). \tag{3.3}$$

At the outlet, the authors applied an absorbing boundary condition which means that there was no reflection form the outlet boundary. Identical conditions were implemented for outlet in the present model. The present numerical results and those obtained in [27] are compared in Fig. 7.

It is seen from the pressure plots that our results match those of [27] well. The blue curve shows the pressure variation in time at the inlet. Thus, we see that the pressure wave travels from the inlet to the midpoint of the parent vessel and then to the outlet of the parent vessel. At the bifurcation, the incident pressure wave, which has a magnitude of about 60 dynes/cm^2, is reflected. Also, at the bifurcation the reflected and incident waves coincide thereby increasing the local pressure. This stepped-up pressure wave then travels through the daughter vessels. At the same time, the reflected wave (from the bifurcation) travels backwards towards the inlet and reaches the midpoint and then finally the inlet of the parent vessel. We see that the magnitude of the reflected wave is 30 dynes/cm^2. This is consistent with the fact that pressure at the parent outlet is the sum of the incident and reflected pressure waves. It is also seen that the reflected wave is half the magnitude of the incident wave which is again according to our calculations that the reflection coefficient is 0.5.

https://doi.org/10.4208/cicp.160114.120914a Published online by Cambridge University Press

Some numerical dispersion appears in the waveforms. The use of more complex numerical schemes, like those shown by Müller et al. (2013) [28], is a possible way of diminishing or eliminating such errors.

4 Results

4.1 Model geometry

As the model validations of Section 3 already provide some insightful results, in this section the 1-D modeling technique is applied to a representative arterial system and approximate results are compared to 3-D results obtained in [26]. Specifically, a transient elastic 3-D model of the representative hepatic arterial system up to the daughter-vessels of the left and right hepatic arteries (Fig. 8) was considered. The anatomy and geometric dimensions of the model as shown in Table 1 were obtained from the most common configuration of the hepatic arterial system based on literature studies [29].

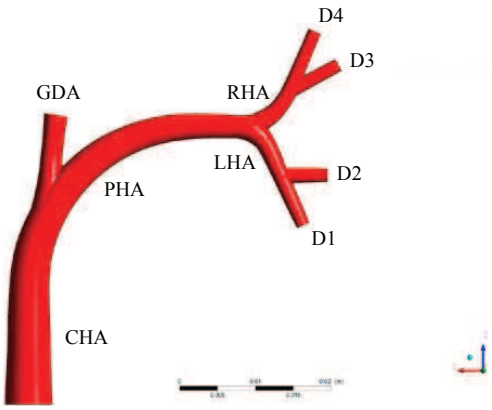


Figure 8: Representative 3-D hepatic arterial system.

The walls of the 3-D system were assumed to be hyperelastic, considering a second-order Yeoh model and a thick-walled cylinder [26]. It should be noted that this relation results in a different variation of elasticity (based on the applied pressure) than that is being used in our 1-D model.

4.2 Boundary conditions

At the inlet, a fully developed parabolic profile was prescribed. The average velocity of this profile was based on the flow waveform of Fig. 9, again obtained from population data [29].

As outlet boundary conditions for GDA, D1, D2, D3 and D4, a WK2 model was used. The Quemada model was adopted for non-Newtonian blood viscosity and a density of 1060 kg/m^3.

https://doi.org/10.4208/cicp.160114.120914a Published online by Cambridge University Press

Table 1: Length and radii of the nine arteries.

	Length (m)	Inlet radius (m)	Outlet radius (m)
CHA	0.02800	0.00300	0.00230
GDA	0.00620	0.00150	0.00150
PHA	0.02700	0.00220	0.00150
RHA	0.00550	0.00125	0.00105
LHA	0.00540	0.00140	0.00110
D4	0.00570	0.00095	0.00085
D3	0.00450	0.00090	0.00085
D2	0.00430	0.00095	0.00085
D1	0.00540	0.00100	0.00085

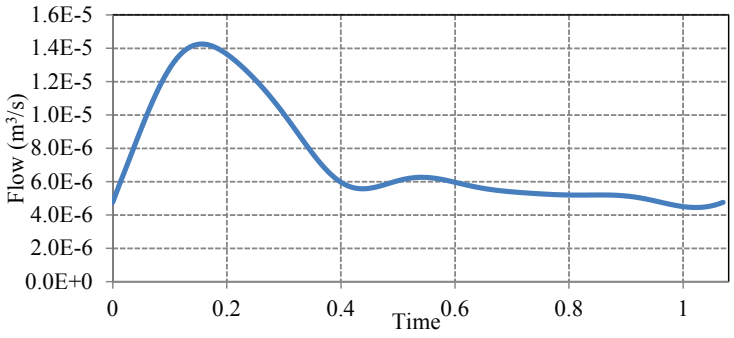


Figure 9: Inlet flow waveform for 3-D and corresponding 1-D simulation.

4.3 Implementation

As the input, the inlet flow waveform as shown in Fig. 9 was prescribed at the inlet of the CHA. The WK2 parameters as shown in Table 2 were used. An effective blood viscosity of 0.0035 Pa.s and a density of 1060 kg/m^3 were used [30].

Table 2: WK2 parameters used in 3-D comparison.

	$R_d \times 10^{10}$ (Pa.s.m^3)	$C \times 10^{12}$ (m^{3}Pa^{-1})
GDA	0.51143	7.249
D1	1.2425	4.463
D2	1.6612	3.156
D3	1.1789	4.390
D4	1.3688	4.131

https://doi.org/10.4208/cicp.160114.120914a Published online by Cambridge University Press

4.4 Fluid flow results

The hyperelastic model used in 3-D simulations implied an elasticity modulus range of 0.3 to 0.5 MPa. Thus, for the 1-D simulation a representative constant elasticity value of 0.4 MPa was implemented for all vessels. Each of the vessels was divided into 30 equal segments. This simulation took about 56 minutes for 4 pulses. The results are given in Figs. 10a-f.

The 1-D pressure and flow rate in space and time match the 3-D results quite well. Still, as for the validation case based on the results of [9], we notice that there is a time-lag in the pressure and flow rate peaks. The flow depends in the pressure gradient in the arteries. So even if the pressure peaks at around 2.4 sec., the pressure gradient is

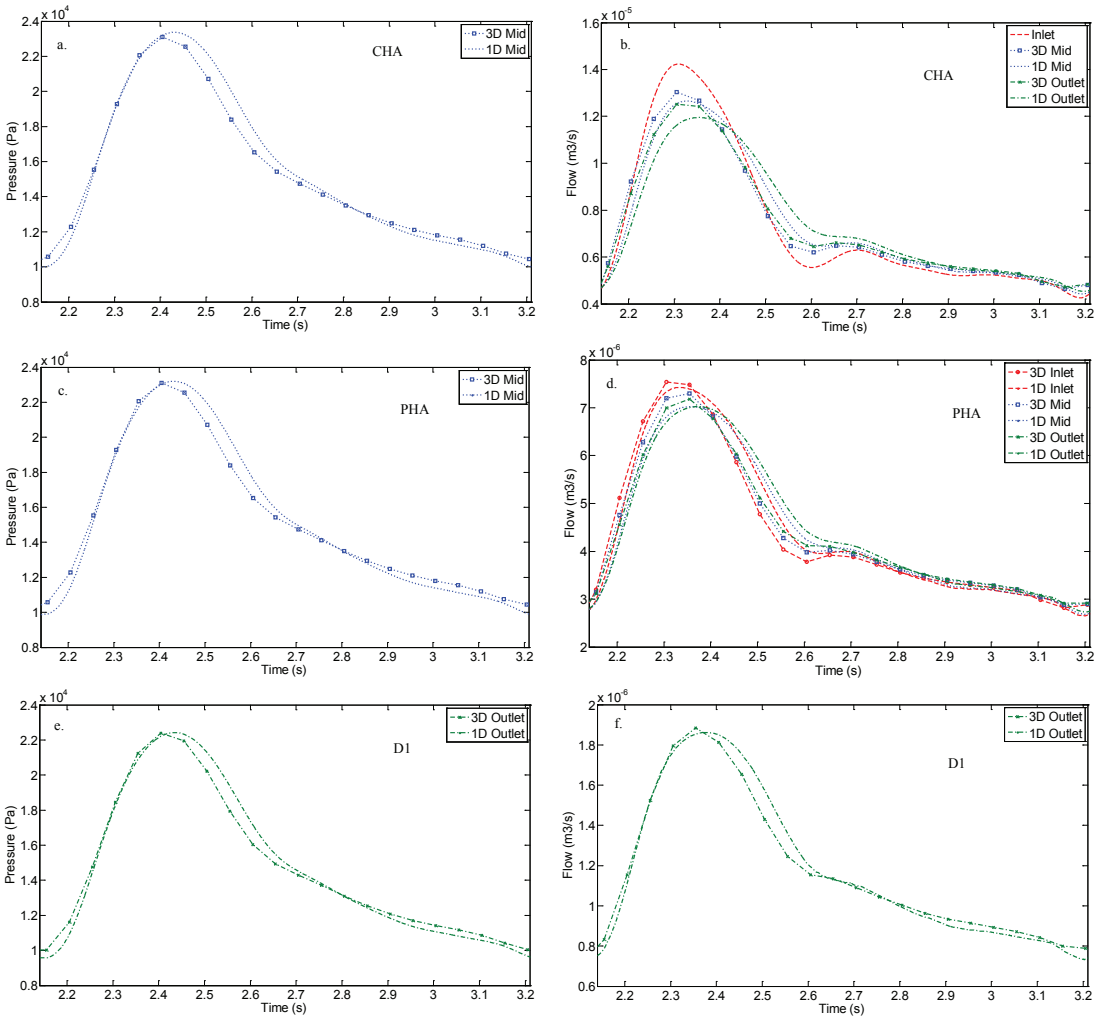


Figure 10: Pressure and Flow for CHA, GDA and D1 for the skewed profile.

https://doi.org/10.4208/cicp.160114.120914a Published online by Cambridge University Press

highest just before that. This is the reason why the peak flow occurs just before the peak pressure.The flow rate in the daughter D1 is seen to be an order of magnitude less than that in the CHA, but the pressures are comparable because the flow area is smaller in D1.

The pulse is made up of two parts — the systole, being the acceleration phase with a peak flow rate, and the diastole, characterized by deceleration and quasi-steady flow. The pulsatility of the flow decreases as it moves further in generations. This is clearly seen when we compare the flow rate results for CHA and D1.

In summary, Figs. 10a-f indicate that a simple 1-D model can predict the same results in terms of flow rates and pressure distributions as those obtained with a sophisticated 3-D simulation. These simulations can be used to predict the particle trajectories on the system.

4.5 Particle transport

Particles used had a diameter of 32 microns and a material density of 1600 kg/m^3. The 3-D model also employed a one-way coupled Lagrangian model to track the particles, which were released with zero-slip velocity, i.e., with a velocity equal to the fluid velocity at the inlet. For both inlet velocity and particle-release distribution, parabolic profiles were assumed. In the 1-D model the initial velocity was the average axial fluid velocity (0.1683 m/s), which is the same for all particles. As all the particles have the same density and radius, they travel as a 1-D cluster and divide among daughter vessels based on the associated flow rates in them. Hence it is opportune to compare the times taken by the particles to exit each of the four daughters obtained form 1-D and 3-D calculations (Fig. 8). Table 3 lists the 1-D and 3-D particle exit times with the skewed velocity profile and using the wall-elasticity model.

Table 3: Particle exit times for skewed profile using exponential elasticity.

	GDA	D1	D2	D3	D4
1-D (s)	0.115	0.172	0.172	0.167	0.170
3-D (s)	0.113	0.1775	0.25	0.18	0.16

In 3-D, the instantaneous velocity of the particles depends on the fluid velocity components at that point. Hence, each particle will have a different velocity and consequently a different exit time. Also, due to the much more complex flow fields, the particles do not take a straight path to the exit but often recirculate and veer off. So, the 3-D exit times in Table 3 are not exact individual particle times but are based on the average time taken by the particles to exit that branch. For this, particles were released over a small time interval at the inlet of CHA. These particles then exit through different branches. For each branch, the exit time required by about half of the total number of particles was calculated. Comparing single trajectories and their exit times could also be an option; but, as mentioned, the particle exit times depend on the fluid velocities and hence the use of a single trajectory would not be representative. It is observed that the particle exit times for

https://doi.org/10.4208/cicp.160114.120914a Published online by Cambridge University Press

1-D are within a 10% error when compared to the 3-D values, except for D2. The reason behind this is that most of the particles exiting D2 were released near the walls where the fluid velocities are lower; thus, causing lower particle velocities and hence higher exit times.

4.6 Particle exit fractions

The number of particles exiting each branch was calculated. The particle distribution across a bifurcation is based on the flow-rate ratio in the daughter branches. Table 4 shows the particle exit fractions in percentages for all the exits for 1-D and 3-D and the corresponding flow rate distribution.

Table 4: Particle exit fractions and average flow distribution for 1-D and 3-D.

Particle exit fractions					
	GDA	D1	D2	D3	D4
1-D (%)	36.96	17.13	12.99	17.46	15.43
3-D (%)	28.7	12.52	15.52	28.51	14.74
Average flow distribution					
1-D (%)	40.34	16.09	12.16	16.90	14.51
3-D (%)	40.38	16.06	12.05	16.92	14.56

The table above show that the 3-D exit flow distribution is correctly predicted by 1-D. We also see that in 1-D, the particle exit fractions are in proportion with the 1-D flow distribution. The numbers will not quite match as Table 4 only shows the average flow distribution, while the actual particle distribution depends on the flow distribution at the particular time when the particles are at the bifurcation. Naturally, the 3-D flow distribution differs from the 3-D particle exit fractions because of the complex geometry and the resulting 3-D flow fields. It should be recalled that the 1-D analysis of the particle distribution across a bifurcation is for a relatively simple geometry, i.e., a rigid bifurcation and straight tubes. Hence the 3-D values are different because of the geometry being viscoelastic and featuring multiple bifurcations with curved tubes, generating complex 3-D flow fields and hence intricate particle paths.

4.7 Computer resources

The 1-D simulations took only around 60 minutes on a PC with 2.67 GHz and 6 GB RAM for the same amount of pulses as that of the 3-D runs. However, the 3-D simulations required about 4 days on a workstation with 40GB of RAM and using 10 processors with 3.33 GHz. Thus, to obtain very similar fluid-particle dynamics results for a bifurcating network, the present 1-D simulation model requires significantly less run time and computer resources than 3-D calculations.

https://doi.org/10.4208/cicp.160114.120914a Published online by Cambridge University Press

5 Conclusions and future work

5.1 Conclusions

Blood flow in arteries is a rather complex phenomenon, involving various factors and parameter values such as blood pulsatility, patient-specific 3-D geometry, artery tethering, blood viscosity, multiple bifurcations, and wall elasticity. A 3-D model simulating all the intricacies of the geometry and involving all the complex phenomena would be very time and computer-resources consuming. For example, in applications such as tumor targeting with drug-particles or radioactive microspheres [1], it is required to model and simulate transport phenomena deep into the arterial system and gain useful results as quickly as possible.

A simple and cost-effective way to do this is using a 1-D model for simulation of arterial pressures and flow rates. In developing such a 1-D model, a number of assumptions were carefully made so as to preserve the physical phenomena and at the same time reduce computational times and resources. These assumptions involve the use of a simple algebraic pressure-area relation, an exponential elasticity model for the vessels and considering only unidirectional flow with a representative skewed velocity profile. However, there is a limit to the number of generations that can be modeled, even in 1-D. Thus, suitable physiological boundary conditions are required to be set up in order to account for the impact of generations further downstream.

The present 1-D model was successfully validated against data sets from the open literature. We implemented a realistic, average, skewed velocity profile in the model. This was based on a representative velocity profile after bifurcation of the vessels. The generalized (skewed) velocity profile, influencing the momentum correction factor as well as the axial friction term, was able to match data sets correctly. The results depend on the elastic model of the vessel used. Similarly, the outlet pressure and flow rates have to be known so as to correctly simulate the downstream conditions.

The 1-D model was augmented with Lagrangian particle transport. This allows for predicting particle distributions across bifurcations and particle travel times. It could also be employed to generate fluid-particle dynamics results for inhaled toxic or therapeutic aerosols.

The 1-D model is a faster tool to predict the flow field variables in the arterial or pulmonary system as compared to the 3-D model. It is not memory intensive and can be run on a regular PC. Apart from being fast, it also produces somewhat equally reliable results. Specifically, we successfully developed and tested a physiological 1-D model that can predict the fluid flow, pressure level and particle trajectory in the arterial system. This model can now be used as an extension to any 3-D model; thus, increasing the reach in terms of the number of downstream generations.

In summary, the specific novel contributions are:

- Particle tracking in arteries is being done with 1-D fluid modeling for the first time.

https://doi.org/10.4208/cicp.160114.120914a Published online by Cambridge University Press

- An average skewed profile was selected based on 3-D simulation of a bifurcation. This representative profile provides better values for the friction and inertia terms in a flow system with bifurcations.

- The 1-D model can be coupled to a 3-D model and simulations can be run for a higher number of generations in vascular or lung-airway systems.

5.2 Limitations and future work

There are, however, some improvements that can be made concerning the core model:

1. A superior numerical scheme, preferably a finite element method with lower dispersion errors, should be explored.

2. The outlet BCs require some knowledge of the pressures and flow rates in the downstream vessels. The more complex impedance BC [5] is an option; but it too, at a point, requires the knowledge of total hydraulic resistance downstream.

3. The particle exit fractions are somewhat off from the 3-D results. A better criterion can be formulated for particle distributions across bifurcations. For example, coefficients considering recirculation and other 3-D effects affecting particle trajectories could be introduced in the particle trajectory equation.

4. The application of this model to lung airways should be appropriate. For lung airways, the pressure-area relation is not the same as that for the systemic arteries. The diameter does not change isentropically with the lung volume [31]. Another tube law for the lung airways and elasticity based on the soft and cartilage tissue content are given in [32].

References

[1] Kleinstreuer C., Basciano C. A., Childress E. M., Kennedy A. S., A new catheter for tumor-targeting with radioactive microspheres in representative hepatic artery systems. Part I: Impact of catheter presence on local blood flow and microsphere delivery, Journal of Biomechanical Engineering, 134:051004-10, 2012.
[2] Childress E. M., Kleinstreuer C., Kennedy A. S., A new catheter for tumor-targeting with radioactive microspheres in representative hepatic artery systems. Part II: Solid tumor-targeting in a patient-inspired hepatic artery system, Journal of Biomechanical Engineering, 134:051005-10, 2012.
[3] Lin C.-L., Tawhai M. H., McLennan G, Hoffman E. A., Multiscale simulation of gas flow in subject-specific models of the human lung, IEEE Engineering in Medicine and Biology Magazine, 28(3):25-33, 2009.
[4] Formaggia L., Gerbeau J. F., Nobile F., Quarteroni A., On the coupling of 3D and 1D Navier-Stokes equations for flow problems in compliant vessels, Computer Methods in Applied Mechanics and Engineering, 191(6-7):561-582, 2001.

https://doi.org/10.4208/cicp.160114.120914a Published online by Cambridge University Press

[5] Olufsen M. S., Modeling the Arterial System with Reference to an Anesthesia Simulator, Ph.D. Thesis, 1998.
[6] Formaggia L., Lamponi D., Quarteroni A., One dimensional models for blood flow in arteries, Journal of Engineering Mathematics, 47:251-276, 2003.
[7] Alastruey J., Parker K. H., Peiro J., Byrd S. M., Sherwin S. J., Modeling the circle of Willis to assess the effects of anatomical variations and occlusions on cerebral flows, Journal of Biomechanics, 40:1794-1805, 2007.
[8] van de Vosse F.N., Stergiopulos N., Pulse wave propagation in the arterial tree, Annual Review of Fluid Mechanics, 43:467-499, 2011.
[9] Kung E., Les A., Figueroa A., Medina F., Arcaute K., Wicker R., McConnell M., Taylor C., In vitro validation of finite element analysis of blood flow in deformable models, Annals of Biomedical Engineering, 39(7):1947-1960, 2011.
[10] Matthys K. S., Alastruey J., Peiró J., Khir A. W., Segers P., Verdonck P. R., Parker K. H., Sherwin S. J., Pulse wave propagation in a model human arterial network: assessment of 1-D numerical simulations against in vitro measurements, Journal of Biomechanics, 40(15):3476-86, 2007.
[11] Segers P., Duboins F., De Wachter D., Verdonck P., Role and relevancy of a cardiovascular simulator, Journal for Extracorporeal Circulation, 3(1):48-56, 1998.
[12] Sherwin S., Franke V., Peiro J., Parker K., One-dimensional modeling of a vascular network in space-time variables, Journal of Engineering Mathematics, 47(3-4):217-250, 2003.
[13] Alastruey J., Numerical modeling of pulse wave propagation in the cardiovascular system: development, validations and clinical applications, Ph.D. Thesis, Imperial College London, London, UK, 2006.
[14] Olufsen M. S., Peskin C. S., Kim W. Y., Pedersen E., Nadim A., Larsen J., Numerical simulation and experimental validation of blood flow in arteries with structured-tree outflow conditions, Annals of Biomedical Engineering, 28:1281-1299, 2000.
[15] Smith N. P., Pullan A. J., Hunter P. J., An anatomically based model of transient coronary blood flow in the heart, SIAM Journal of Applied Mathematics, 62:990-1018, 2002.
[16] Ho H., Sands G., Schmid H., Mithraratne K., Mallinson G., Hunter P., A hybrid 1D and 3D approach to hemodynamics modelling for a patient-specific cerebral vasculature and aneurysm, Medical Image Computing and Computer-Assisted Intervention – MICCAI Part II Lecture Notes in Computer Science, 5762:323-30, 2009.
[17] Reymond P., Merenda F., Perren F., Rufenacht D., Stergiopulos N., Validation of a one-dimensional model of the systemic arterial tree, American Journal of Physiology-Heart and Circulatory Physiology, 297:H208-H222, 2009.
[18] Wang J. J., Parker K. H., Wave propagation in a model of the arterial circulation, Journal of Biomechanics, 37:457-470, 2004.
[19] Umbarkar T., Computationally Efficient Simulation of Fluid-Particle Flow in Elastic Bifurcating Systems, MS Thesis, NC State University, Raleigh, NC, 2013.
[20] Bushi D., Grad Y., Einav S., Yodfat O., Nishri B., Tanne D., Hemodynamic evaluation of embolic trajectory in an arterial bifurcation: An in-vitro experimental model, Stroke, 36:2696-2700, 2005.
[21] Pedley, T. J., Schroter, R. C., Sudlow, M. F., Flow and pressure drop in systems of repeatedly branching tubes, Journal of Fluid Mechanics, 46:365-383, 1971.
[22] Stergiopulos N., Young D. F., Rogge T. R., Computer simulation of arterial flow with application to arterial and aortic stenoses, Journal of Biomechanics, 25(12):1477-1488, 1992.
[23] Olufsen M. S., Structured tree outflow condition for blood flow in larger systemic arteries,

https://doi.org/10.4208/cicp.160114.120914a Published online by Cambridge University Press

American Journal of Physiology, Heart and Circulatory Physiology, 276:H257-268, 1999.
[24] Basciano C., Computational Particle-Hemodynamics Analysis Applied to an Abdominal Aortic Aneurysm with Thrombus and Microsphere-Targeting of Liver Tumors, Ph.D. Thesis, NC State University, Raleigh, NC, USA, 2010.
[25] Schiller L., Naumann A., Über die grundlegenden Berechnungen bei der Schwerkraftaufbereitung, z. Ver. Deut. Ing. 77:318-320, 1933.
[26] Childress E. M., Kleinstreuer C., Impact of fluid-structure interaction on direct tumor-targeting in a representative hepatic artery system, Annals of Biomedical Engineering (in press), 2013.
[27] Marchandise E., Willemet M., Lacroix V., A numerical hemodynamic tool for predicative vascular surgery, Medical and Engineering Physics, 31:131-144, 2009.
[28] Müller L. O., Parés C., Toro E. F., Well-balanced high-order numerical schemes for one-dimensional blood flow in vessels with varying mechanical properties, Journal of Computational Physics, 242:53-85, 2013.
[29] Basciano C. A., Kleinstreuer C., Kennedy A. S., Dezarn W. A., Childress E., Computer modeling of controlled microsphere release and targeting in a representative hepatic artery system, Annals of Biomedical Engineering, 38(5):1862-79, 2010.
[30] Waite L., Fine J., Applied Biofluid Mechanics, The McGraw-Hill Companies, Inc., ISBN 9780071472173, 2007.
[31] Brown R. H., Mitzner W., Effect of lung inflation and airway muscle tone on airway diameter in vivo, Journal of Applied Physiology, 80:1581-1588, 1996.
[32] Alhamadi E. S., 1D Model for Flow in the Pulmonary Airway System, Ph.D. Thesis, The University of Manchester, Manchester, UK, 2012.
[33] Martin V., Clement F., Decoene A., Gerbeau J-F., Parameter identification for a one-dimensional blood flow model, ESIAM: Proceedings, 14:174-200, 2005.
[34] Quarteroni A., Formaggia L., Veneziani A., Cardiovascular Mathematics, Springer-Verlag, Italia, Milano, 2009.
[35] Loth, E. and Dorgan, A. J., An equation of motion for particles of finite Reynolds number and size, Environ. Fluid Mechanics, 9(2):187-206, 2009.

https://doi.org/10.4208/cicp.160114.120914a Published online by Cambridge University Press